A worldwide analysis of spatiotemporal changes in water balance-based evapotranspiration from 1982 to 2009

Zhenzhong Zeng, Tao Wang, Feng Zhou, Philippe Ciais, Jiafu M Mao, Xiaoying Shi, Shilong Piao

AGU PUBLICATIONS

JGR

Journal of Geophysical Research: Atmospheres

RESEARCH ARTICLE
10.1002/2013JD020941

Key Points:
- Developed a satellite-based water balance method to estimate global ET
- Significant seasonal and spatial variations exist in global terrestrial ET
- The method improved ET estimations in wet regions and seasons

Correspondence to:
S. Piao,
slpiao@pku.edu.cn

Citation:
Zeng, Z. Z., T. Wang, F. Zhou, P. Ciais, J. F. Mao, X. Y. Shi, and S. L. Piao (2014), A worldwide analysis of spatiotemporal changes in water balance-based evapotranspiration from 1982 to 2009, *J. Geophys. Res. Atmos.*, *119*, 1186–1202, doi:10.1002/2013JD020941.

Received 24 SEP 2013
Accepted 30 DEC 2013
Accepted article online 4 JAN 2014
Published online 6 FEB 2014

A worldwide analysis of spatiotemporal changes in water balance-based evapotranspiration from 1982 to 2009

Zhenzhong Zeng[1], Tao Wang[2], Feng Zhou[1], Philippe Ciais[2], Jiafu Mao[3], Xiaoying Shi[3], and Shilong Piao[1,4]

[1]College of Urban and Environmental Sciences, Peking University, Beijing, China, [2]Laboratoire des Sciences du Climat et de l'Environnement, CEA CNRS UVSQ, Paris, France, [3]Environmental Sciences Division, Oak Ridge National Laboratory, Oak Ridge, Tennessee, USA, [4]Institute of Tibetan Plateau Research, Chinese Academy of Sciences, Beijing, China

Abstract A satellite-based water balance method is developed to model global evapotranspiration (ET) through coupling a water balance (WB) model with a machine-learning algorithm (the model tree ensemble, MTE) (hereafter WB-MTE). The WB-MTE algorithm was firstly trained by combining monthly WB-estimated basin ET with the potential drivers (e.g., radiation, temperature, precipitation, wind speed, and vegetation index) across 95 large river basins (5824 basin-months) and then applied to establish global monthly ET maps at a spatial resolution of 0.5° from 1982 to 2009. The global land ET estimated from WB-MTE has an annual mean of 593 ± 17 mm for 1982–2009, with a spatial distribution consistent with previous studies in all latitudes but the tropics. The ET estimated by WB-MTE also shows significant linear trends in both annual and seasonal global ET during 1982–2009, though the trends seem to have stalled after 1998. Moreover, our study presents a striking difference from the previous ones primarily in the magnitude of ET estimates during the wet season particularly in the tropics, where ET is highly uncertain due to lack of direct measurements. This may be tied to their lack of proper consideration to solar radiation and/or the rainfall interception process. By contrast, in the dry season, our estimate of ET compares well with the previous ones, both for the mean state and the variability. If we are to reduce the uncertainties in estimating ET, these results emphasize the necessity of deploying more observations during the wet season, particularly in the tropics.

1. Introduction

Evapotranspiration (ET) is the flux of water transferred from the land surface to the atmosphere; it plays a central role in driving the climate system [*Trenberth et al.*, 2009]. ET is controlled by a combination of atmospheric evaporative demand, the energy available at the surface, and the soil moisture [*Wang et al.*, 2010]. With sufficient soil moisture, most of the net radiation at the surface is converted into latent heat (ET), controlling the surface temperature. Atmospheric evaporative demand is expected to increase with increasing temperature [*Monteith*, 1981; *Roderick et al.*, 2007; *Sheffield et al.*, 2012]. Thus, in response to global warming, one should expect an intensification (or acceleration) of the global hydrological cycle [*Huntington*, 2006], with an increase in both ET and precipitation [*Douville et al.*, 2013]. Indeed, an increase in global annual land ET over the last two decades of the twentieth century has been documented by several studies [*Jung et al.*, 2010; *Zeng et al.*, 2012; *Zhang et al.*, 2012]. However, this global ET increase may have ceased or slowed down during the past decade [*Jung et al.*, 2010; *Vinukollu et al.*, 2011; *Zeng et al.*, 2012; *Mueller et al.*, 2013]. One mechanism proposed to explain this phenomenon is the increasingly widespread limitation of ET by soil moisture deficit [*Jung et al.*, 2010]. Yet, both how ET has varied over the past decades and what may have caused any variation is still quite uncertain [*Wang et al.*, 2010].

Using satellite and ground-based observations, several approaches have been used to estimate global ET over the past three decades. Among them, only the eddy-covariance (EC) method provides a direct but local in situ measurement of ET [*Baldocchi et al.*, 2001; *Wang and Dickinson*, 2012]. Eddy-covariance measurements can be used to generate ET data sets on a global grid, either by applying statistical models such as machine-learning interpolation algorithms [*Jung et al.*, 2009, 2010], or in process-oriented satellite algorithms, such as the Penman-Monteith equation [*Mu et al.*, 2011], the modified Penman-Monteith equation, and the Priestley-Taylor equation [*Zhang et al.*, 2010]. Using a machine-learning algorithm (a set of linear regressions), *Jung et al.* [2010] (hereafter JUN10)

drew up monthly gridded maps of global land ET from 1982 to 2008, by integrating EC measurements from a global network of 198 flux towers (FLUXNET) with geospatial information from meteorological (precipitation, temperature, and potential radiation) and satellite observations (Fraction of Absorbed Photosynthetically Active Radiation). In addition, eddy-covariance ET measurements have also been employed to parameterize mechanism-based algorithms using satellite data, which were then used to produce ET maps for the period 1983–2006 [*Zhang et al*., 2010] (hereafter ZHA10). However, ET measured using the eddy-covariance method must be treated with caution. First, a lack of energy balance closure is often observed at EC sites, i.e., the sum of the turbulent fluxes of sensible and latent heat and heat storage falls short of the measured available energy at the surface [*Wilson et al*., 2002; *Foken*, 2008]. Second, the EC measurements span a relatively short period and have a sparse spatial coverage, particularly in the Southern Hemisphere and the tropics. These factors create uncertainty when long-term global estimates of ET are produced from short-tern EC records [*Wang and Dickinson*, 2012] with space for time extrapolation biases.

Currently, satellite-based energy balance approaches are frequently used to estimate monthly ET on both regional and global scales [*Fisher et al*., 2009; *Jung et al*., 2010; *Zhang et al*., 2010; *Mu et al*., 2011; *Vinukollu et al*., 2011; *Yan et al*., 2012]. However, there is a significant challenge for these satellite-based energy balance methods, using current remotely sensed radiation as model input to detect ET and its trend over wet regions [*Zhang et al*., 2012]. An alternative is to estimate regional-average ET from the terrestrial water balance; ET is then calculated as the residual between total precipitation and the sum of river discharge and terrestrial water storage change [*Rodell et al*., 2004]. This water balance method (WB) was implemented by *Zeng et al*. [2012] to estimate annual mean ET over large river basins from total precipitation, in situ discharge measurements, and GRACE (Gravity Recovery and Climate Experiment) satellite-based measurements of the change in terrestrial water storage change [*Tapley et al*., 2004]. The recent release of 10 day resolution observations for GRACE satellites [*Bruinsma et al*., 2010] now provides us with the data to estimate basin-scale ET on a monthly time step. In this study, we estimate global monthly ET on a grid of 0.5° resolution by downscaling monthly basin-scale ET using the same machine-learning algorithm (the model tree ensemble, MTE) as *Jung et al*. [2010]. Previous work has shown that empirical and statistical methods can be more accurate at estimating ET than complex physical and analytical methods [*Kalma et al*., 2008], since these former approaches are data driven and less dependent on any rigid theoretical assumptions [*Jung et al*., 2010]. The objectives of this study are to (1) evaluate the performance of a new model that produces ET maps by combining the water balance (WB) approach with a model tree ensemble (hereafter WB-MTE) to estimate ET at the basin level, (2) estimate the spatial distribution of annual and seasonal ET from the WB-MTE algorithm on a global scale, and (3) investigate the trends of global ET at both annual and seasonal timescales from 1982 to 2009.

2. Methods and Data Sets

2.1. Estimate of Basin ET From Surface Water Balance

The CNES/GRGS (Centre National d'Etudes Spatiales/Groupe de Recherches de Géodésie Spatiale) 10 day gravity field models (release 2) provide a global distribution of terrestrial water storage anomaly (TWSA) by recalculating GRACE measurements of geopotential solutions at 10 day intervals, based on an improved data editing and solution-regulation procedure [*Bruinsma et al*., 2010]. For a given river basin, the monthly terrestrial water storage change (TWSC) is calculated as the difference between the final 10 day TWSA of the month and the first 10 day TWSA of the month at the same location. At a large river basin scale, one can safely assume that the boundary of the surface drainage watershed coincides with the boundary of the groundwater flow [*Rodell et al*., 2004] so that we can ignore the possibility of groundwater being diverted to another basin. Therefore, the monthly basin water balance equation can be expressed as follows:

$$\mathrm{ET}(n) = P(n) - Q(n) - \left(\overline{\mathrm{TWSA}_{\mathrm{End}}(n)} - \overline{\mathrm{TWSA}_{\mathrm{First}}(n)}\right) \quad (1)$$

where n is the month; ET, P, and Q are ET (mm per month), precipitation (mm per month), and discharge (mm per month), respectively; $\overline{\mathrm{TWSA}_{\mathrm{End}}(n)}$ ($\overline{\mathrm{TWSA}_{\mathrm{First}}(n)}$) is the final (first) 10 day TWSA of the month at the location (mm). On a monthly time step, TWSC cannot be neglected since it is in the same order of magnitude as ET, especially for those basins with relatively low ET values [see *Zeng et al*., 2012]. Equation (1) is used to calculate monthly basin ET between 2002 and 2009, using precipitation from rain gauge stations, river discharge from hydrological stations, and TWSA from GRACE data. Monthly ET is set to zero if the calculated ET from equation (1)

Table 1. List of Explanatory Variables Used for Training the Model Tree Ensembles (MTE)[a]

Variable	Type	Type of Variability	Source
Temperature	Regression	Monthly	CRU
Precipitation (Pre)	Regression	Monthly	CRU
Incoming radiation (Rad)	Regression	Monthly	CRU-NCEP
Pressure	Regression	Monthly	CRU-NCEP
Vapor pressure	Regression	Monthly	CRU
Wind speed	Regression	Monthly	CRU-NCEP
Wet day frequency	Regression	Monthly	CRU
Frost day frequency	Regression	Monthly	CRU
Normalized Difference Vegetation Index (NDVI)	Regression	Monthly	AVHRR
Mean annual NDVI (ANDVI)	Split	Static	AVHRR
Mean monthly NDVI (MNDVI)	Split	Monthly but static over years	AVHRR
Mean annual precipitation (AP)	Split	Static	CRU
Mean annual radiation (AR)	Split	Static	CRU-NCEP
Mean monthly precipitation (MP)	Split	Monthly but static over years	CRU
Mean monthly radiation (MR)	Split	Monthly but static over years	CRU-NCEP
Dry season length	Split	Static	CRU
IGBP vegetation type	Split	Static	MODIS
NDVI × Pre	Split and regression	Monthly	
NDVI × Rad	Split and regression	Monthly	
NDVI × Pre × Rad	Split and regression	Monthly	
ANDVI × AP	Split	Static	
ANDVI × AR	Split	Static	
ANDVI × AP × AR	Split	Static	
MNDVI × MP	Split	Monthly but static over years	
MNDVI × MR	Split	Monthly but static over years	
MNDVI × MP × MR	Split	Monthly but static over years	

[a]In "Type" column, "Regression" denotes the variable used for regression, and "Spilt" represents the variable used for data stratification. In "Type of variability" column, "Monthly" variables are continuously updated for each month, and "static" variables remain the constant across all months and years. "Monthly but static over years" variables change monthly, but the monthly values are repeatedly used across all years.

is less than zero or if maximum temperature of that month is lower than 0°C. This filter might underestimate basin ET because it neglects snow sublimation and evapotranspiration from subregions where the temperature is below freezing (see Figure 3d). In addition, we also exclude monthly basin ET, if it is higher than the highest monthly ET inferred from the water balance equation on the three tropical rainforest basins in this study (Amazon, Tocantins, and Rio Parnaiba).

2.2. Estimate of Global ET

We use the same MTE algorithm as *Jung et al*. [2009, 2010] to estimate gridded land ET on a monthly time step. The MTE was first trained with monthly basin-average ET estimated from the surface water balance (WB) as the independent variable and the set of ET explanatory variables listed in Table 1 as inputs. We then extended the trained MTE (i.e., WB-MTE) developed for our basins (see Figure 1) to a global domain. For each vegetated land pixel (0.5° in our case), monthly ET is estimated from the trained MTE based on monthly climate and satellite remote sensing data (Table 1) during the period from 1982 to 2009. In addition, the pixels where WB-MTE estimated ET was higher than the highest WB-estimated monthly basin ET (about 0.5% of global domain) were also excluded from the analysis. The MTE technique is an efficient method to upscale carbon and water fluxes from the site level to the regional (or global) level and performs better than a single tree in terms of extrapolation (see *Jung et al*. [2009, 2010] for detailed description of MTE). In this study, the estimate of ET at the pixel level is achieved by downscaling WB-estimated basin ET; this is in contrast to the previous study which used an upscaling method to derive gridded ET from point EC measurements [*Jung et al*., 2010]. To evaluate the capability of the downscaling approach, WB-MTE simulated ET aggregated from the pixels within each basin was compared to WB-estimated basin ET (see Figures 2a and 3). In this study, the trends of ET are estimated by nonparametric Mann-Kendall test, as used for detection of monotonic trends in environmental time series [*Jung et al*., 2010; *Dorigo et al*., 2012].

2.3. Data

The monthly basin-average ET is calculated as the difference between total precipitation and the sum of river discharge and basin-averaged TWSC. Precipitation data is from the Climatic Research Unit (CRU) TS 3.1 data

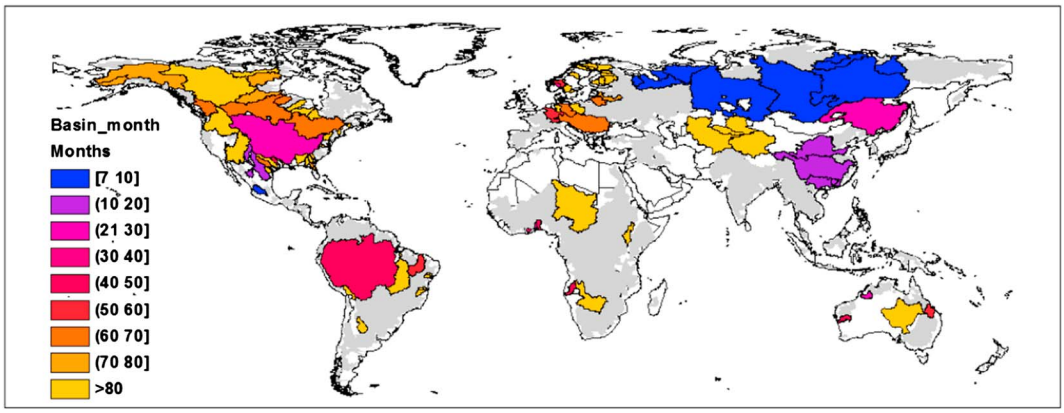

Figure 1. Map of basins used in this study. The color refers to the number of months at each basin that has passed the quality control and been included in the analysis.

[*Mitchell and Jones*, 2005]. Both the digital map of world river basins and discharge data during the period 2002–2009 are from the Global Runoff Data Centre [*GRDC*, 2007]. Since 2008, CNES/GRGS has provided 10 day TWSA data with a spatial resolution of 1°×1°, i.e., the version 2 of the CNES/GRGS time-variable gravity field models based on the GRACE data (GRACE/LAGEOS, http://grgs.obs-mip.fr/grace/variable-models-grace-lageos/grace-solutions-release-02) [*Bruinsma et al.*, 2010]. These gridded TWSA data are used to obtain monthly basin TWSC. River basins were excluded from this study if their area is less than 10,000 km^2 (a pixel of about of 1°×1°) or if GRDC [*GRDC*, 2007] lacks their discharge data for the period 2002–2009. In

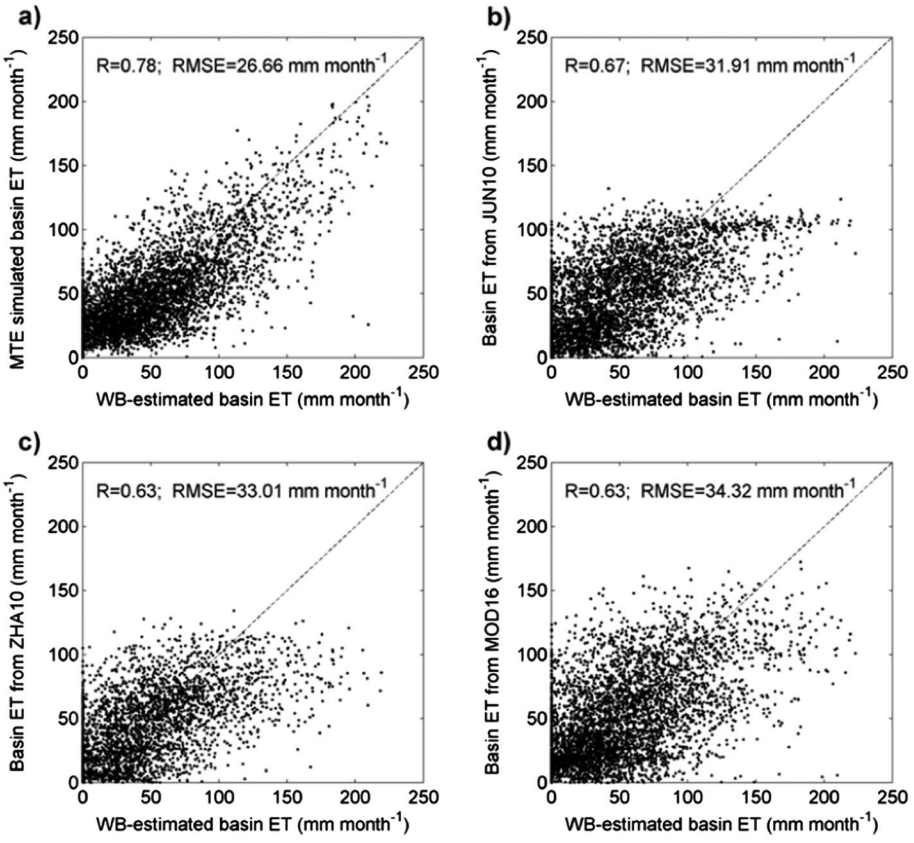

Figure 2. Comparison of modeled and WB-estimated monthly evapotranspiration (ET) at the basin level (n = 5824 basin × months): (a) WB-MTE ET, (b) JUN10 ET, (c) ZHA10 ET, and (d) MOD16 ET.

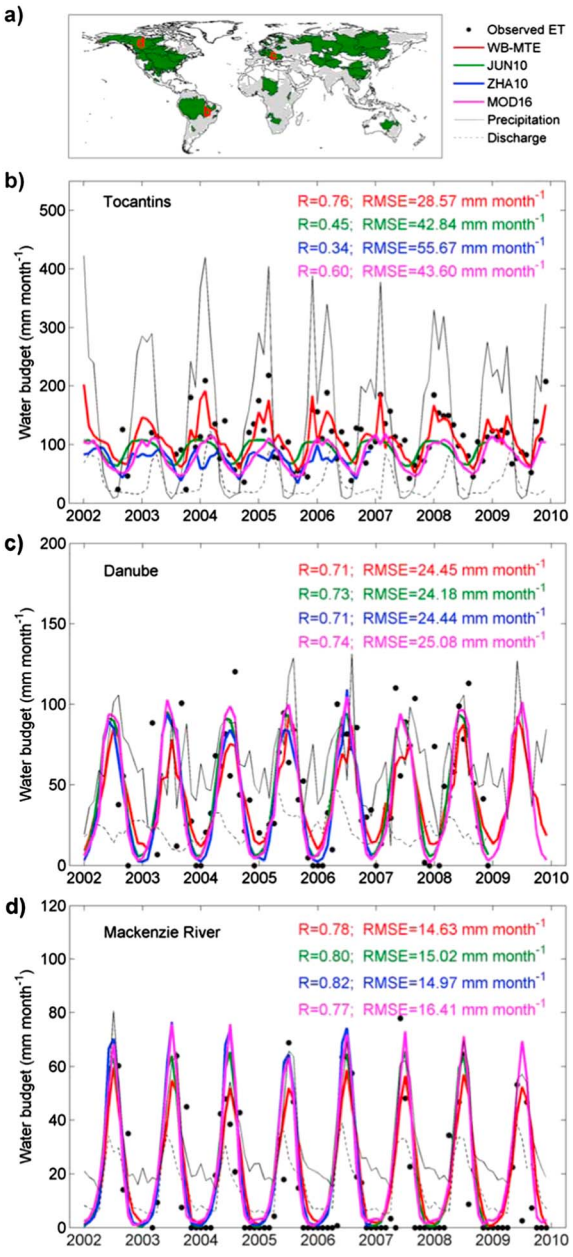

Figure 3. (a) The locations of the three basins. The monthly time series comparison of WB-estimated ET and four ET estimates (WB-MTE, JUN10, ZHA10, and MOD16) at three representative basins: (b) Tocantins basin at low latitude, (c) Danube basin at middle latitude, and (d) Mackenzie River basin at high latitude. Also shown are precipitation and discharge at the basin level.

total, 95 large basins (a total of 5824 basin-months) were retained for the analysis (Figure 1); this covers 50% of the global land basin area and 45% of the precipitation falling on that land.

Meteorological variables were interpolated from weather station data from CRU TS3.1 [*Mitchell and Jones*, 2005] and the CRU-NCEP product (http://dods.extra.cea.fr/data/p529viov/cruncep); these were used to construct the MTE for the estimation of monthly gridded land ET. These variables include temperature, precipitation, radiation, pressure, vapor pressure, wind speed, wet day frequency, and frost day frequency (see Table 1) [*Penman*, 1948; *Thornthwaite*, 1948; *Roderick et al*., 2007; *Teuling et al*., 2009; *Jung et al*., 2010; *Fisher et al*., 2011; *McVicar et al*., 2012; *Sheffield et al*., 2012]. CRU-NCEP is a climate data set generated by adding to the CRU TS3.1 monthly climate data from the submonthly normalized variability of the NCEP reanalysis [*Kanamitsu et al*., 2002]. Solar radiation is a key variable driving ET, especially in regions where soil moisture is nonlimiting [*Hutyra et al*., 2007; *Fisher et al*., 2009; *Costa et al*., 2010]. Given that solar radiation is not provided in CRU TS3.1, we used solar radiation from CRU-NCEP instead. Vegetation type has been suggested as an important determinant for ET [*Piao et al*., 2007], and normalized difference vegetation index (NDVI) is used as a proxy for the physiological and structural characteristics of vegetation [*Myneni et al*., 1998]. NDVI data with a spatial resolution of 8 km during the period 1982–2009 are generated from the Global Inventory Modeling and Mapping Studies (GIMMS) group at NASA GSFC [*Tucker et al*., 2005]. The dry season length for a given pixel is calculated as the sum of those continuous months with multiyear average precipitation $\leq$30% of multiyear mean total annual precipitation [*Staver et al*., 2011]. The vegetation type is derived from the Moderate Resolution Imaging Spectroradiometer (MODIS) land cover type product (version 5 of MCD12Q1) [*Cohen et al*., 2006], and it is assumed to remain constant during the period of analysis.

Three published global monthly ET products, i.e., JUN10, ZHA10, and MODIS ET [*Mu et al*., 2011] (hereafter MOD16), were used for comparison in this study. As described above, *Jung et al*. [2010] provided a global ET product at a 0.5° resolution from 1982 to 2008 by combining EC measurements, meteorological and satellite observations, and a machine-learning algorithm (MTE). Both ZHA10 and MOD16 ET products were derived from *Numerical Terradynamic Simulation Group* (NTSG; www.ntsg.umt.edu/). ZHA10 is a global ET product at 8 km resolution from 1983 to 2006. The global ET algorithm used by ZHA10 estimates plant transpiration and

soil evaporation using a modified Penman-Monteith approach with an NDVI-based canopy conductance model, which is parameterized using regional EC measurements [*Zhang et al*., 2010]. This algorithm also quantifies open water evaporation using a Priestley-Taylor approach [*Zhang et al*., 2010]. MOD16 is a regular 1 km^2 ET data set for vegetated areas across the globe at 8 day intervals from 2000 to 2010. The MODIS ET algorithm uses a Penman-Monteith approach driven by MODIS derived albedo, land cover, leaf area index, enhanced vegetation index, and daily meteorological inputs including incoming solar radiation, surface air temperature, air pressure, and air humidity from NASA's Global Modeling and Assimilation Office [*Mu et al*., 2011]. The MODIS ET algorithm is also parameterized using tower EC measurements [*Mu et al*., 2011]. To compare the capability of these algorithms at capturing the magnitude and variability of WB-estimated basin ET, we compared our WB-estimated ET with modeled ET at basin scale for our WB-MTE algorithm and the three ET products (see Figures 2 and 3). Note that the main objective of the intercomparison of different ET products is not to demonstrate which product is more accurate but rather to find out when and where the discrepancies occur across different products (see Figures 7 and 8).

3. Results

3.1. Evaluation of WB-MTE Performance in Estimating Basin ET

In this study, the monthly basin ET derived from the water balance approach (equation (1)) (hereafter WB-estimated basin ET) can be regarded as reliable since rain gauge station data for precipitation, in situ river discharge, and satellite-based TWSC are used as inputs [*Zeng et al*., 2012]. At the monthly timescale, our analysis shows that the WB-MTE-based ET reconstruction is comparable to WB-estimated ET across all 5824 basin-months, with a nearly zero mean bias (−0.03 mm per month) and a root mean square error (RMSE) of 26.7 mm per month (Figure 2a).

A statistical comparison of WB-estimated and modeled basin ET for the WB-MTE algorithm and three other published ET products (JUN10, ZHA10, and MOD16) indicates that the WB-MTE algorithm is the most accurate at reproducing WB-estimated basin ET, in terms of correlation coefficient (R) and RMSE. Our WB-MTE product has a higher R (0.78) and lower RMSE (26.7 mm per month) (Figure 2a) than the other three data products ($R = 0.63 \sim 0.67$; RMSE = 33.01 ~ 34.32 mm per month, Figures 2b, 2c, and 2d). More importantly, the WB-MTE algorithm works better for basins with high ET values, where ET tends to be underestimated by the three other products (see Figure 2).

To further illustrate the performance of the WB-MTE algorithm, the monthly variations of ET from 2002 to 2009 are shown for three representative basins, spanning latitudes from tropical to Arctic: the Tocantins, Danube, and Mackenzie River basins (Figures 3b–3d). As shown in Figure 3, the monthly variations of ET over these three basins are well captured by the WB-MTE algorithm, with RMSE ranging from 14.6 to 28.6 mm per month and R from 0.71 to 0.78. This comparison reveals that in terms of R and RMSE the WB-MTE algorithm and the other three ET data products are more consistent between each other for the Danube and Mackenzie River basins (Figures 3c and 3d) than for the Tocantins one (Figure 3b). For the Tocantins basin, if we consider as an index of variability the standard deviation of monthly ET, it follows that the "true" ET variability from the WB approach is 43.9 mm per month, which is underestimated by JUN10, ZHA10, and MOD16 (range 16.0 ~ 22.8 mm per month), whereas the WB-MTE result provides a closer approximation (33.9 mm per month). The reason for this is that the WB-MTE algorithm can better reproduce the WB-estimated ET during December to March when precipitation is greatest. For example, the WB-estimated ET over the Tocantins basin can be as high as 150 ~ 200 mm per month from December to March, which is well captured by the WB-MTE algorithm but underestimated by the other reconstructions (100 ~ 120 mm per month).

3.2. Spatially Averaged ET

Using the MTE trained with WB-estimated basin mean ET and geospatial within-basin information from satellite remote sensing and climate data, we estimated global monthly gridded ET at a spatial resolution of 0.5° from 1982 to 2009. The multiyear (1982–2009) average global annual land ET weighted by area is 593 ± 17 mm yr^{-1} (a total volume of $71.1 \pm 2.1 \times 10^3$ km^3). This is almost the same value as was obtained with a WB-based approach (604 ± 46 mm yr^{-1}) [*Zeng et al*., 2012] but higher than JUN10 ($65 \pm 3 \times 10^3$ km^3 yr^{-1} during 1982–2008), ZHA10 (539 ± 9 mm yr^{-1} during 1982–2006), and MOD16 (552 ± 4 mm yr^{-1} during 2000–2010). Moreover, the multiyear-average global annual ET from this study amounts to 581 ± 14 mm yr^{-1} during

1989–1995, a value that falls within the range (511 ~ 650 mm year^{-1}) estimated from 30 diagnostic ET data sets from observations and 11 data sets from land surface models [*Mueller et al*., 2011].

On the seasonal timescale, the multiyear (1982–2009) average global land ET during MAM (March, April, and May), JJA (June, July, and August), SON (September, October, and November), and DJF (December, January, and February) are 47.4, 61.4, 46.9, and 40.5 mm per month, respectively. This seasonality is similar in phase and amplitude but higher in magnitude than the other three data sets. For example, during JJA and DJF, their estimates are within the range of 55 ~ 61 and 32 ~ 36 mm per month, respectively.

3.3. Mean Spatial Pattern of ET

3.3.1. Annual

Both the multiyear (1982–2009) average annual ET spatial distribution and its zonal average are shown in Figure 4a. We find that ET varies among regions and latitudes, yet with a maximum between 23°S and 23°N. Highest annual ET occurs in the tropics and lowest values in the Arctic. This is because at high latitudes ET is limited by low solar radiation and freezing temperatures over much of the year. As shown in Figure 4a, the latitudinal distribution of ET from our MTE-WB estimate agrees with those of JUN10 and ZHA10. Nevertheless, our ET estimate is higher than that from JUN10 and ZHA10 particularly in the tropics (Figure 4a).

3.3.2. Seasonal

Figures 4b–4e displays multiyear (1982–2009) seasonal patterns of global land ET. Distinct seasonal cycles of ET can be found north of 30°. For example in the Northern Hemisphere, mean monthly ET from WB-MTE is higher during JJA when air temperature, solar radiation, and NDVI (as a surrogate of active transpiring canopies) are maximal (data not shown). During SON and DJF, monthly ET rates are smaller, reflecting plant dormancy because of decreasing air temperatures and low solar energy. By contrast, ET around the equator is high throughout the whole year. High ET is also found in South America, Africa, and Southeast Asia, where tropical rainforests prevail.

We also found that the locations where peak ET rates occur differ among the four seasons (Figures 4b–4e). For example, during MAM and SON, peak ET occurs around the equator (Figures 4b and 4d). Peak ET then moves northward to the Tropic of Cancer during JJA (Figure 4c) and southward to the Tropic of Capricorn during DJF (Figure 4e). The seasonal variation in locations where peak ET occurs coincides with the development and the movement of the Intertropical Convergence Zone, where higher precipitation generally occurs.

We obtain a similar latitudinal distribution of ET between our estimate and the previous two approaches (JUN10 and ZHA10) across the four seasons (Figures 4b–4e). However, the seasonal change in the locations where peak ET rates occur (within 23°S and 23°N) is not obvious in the previous two estimates. Moreover, our ET estimate is obviously higher than those from JUN10 and ZHA10 in the locations where peak ET rates occur, particularly during JJA and DJF (Figures 4c and 4e).

3.4. Characteristics of ET Trends

3.4.1. Annual

As shown in Figure 5a, the global annual land ET increased from 1982 to 2009 with a linear fit having a slope of 1.5 mm yr^{-2} ($p < 0.001$). This increase of global annual land ET mainly occurred between 1982 and 1998, with a linear trend of 2.2 mm yr^{-2} ($p < 0.01$). Such an increase in annual ET is consistent with the expected acceleration of the global terrestrial hydrological cycle in response to global warming [*Huntington*, 2006; *Douville et al*., 2013]. However, since 1998, the increase in global annual ET appears to have stalled ($p = 0.45$), with a 95% confidence interval trend in the range $-1.3 \sim 2.0$ mm yr^{-2}. This stabilization of ET seems to be driven by trend changes in the Southern Hemisphere (SH) more than in the Northern Hemisphere (NH). In the SH, the ET time slope is found to have changed from positive (20.0 mm yr^{-1} per decade) during 1982–1998 (pre-1998) to negative (-3.8 mm yr^{-1} per decade) during 1998–2009 (post-1998) (Figure 5a). In the NH, a significant ET increase in the pre-1998 period (19.2 mm yr^{-1} per decade, $p < 0.01$) has become nonsignificant in the post-1998 period (11.7 mm yr^{-1} per decade, $p = 0.15$).

3.4.2. Seasonal

Figures 5b–5e shows interannual variations of global land ET for the four seasons (DJF, MAM, JJA, and SON). We found significant ET increases at a rate of 0.10, 0.13, 0.13, and 0.14 mm month^{-1} yr^{-1} from 1982 to 2009 for DJF, MAM, JJA, and SON, respectively. All periods except MAM show a significant positive trend ($p < 0.1$) before 1998, but these positive trends cease ($p > 0.1$) after 1998 (Figures 5b–5e). For example, in JJA, global ET significantly increased at a rate of 0.2 mm month^{-1} yr^{-1} between 1982 and 1998 ($p < 0.05$), but there is no

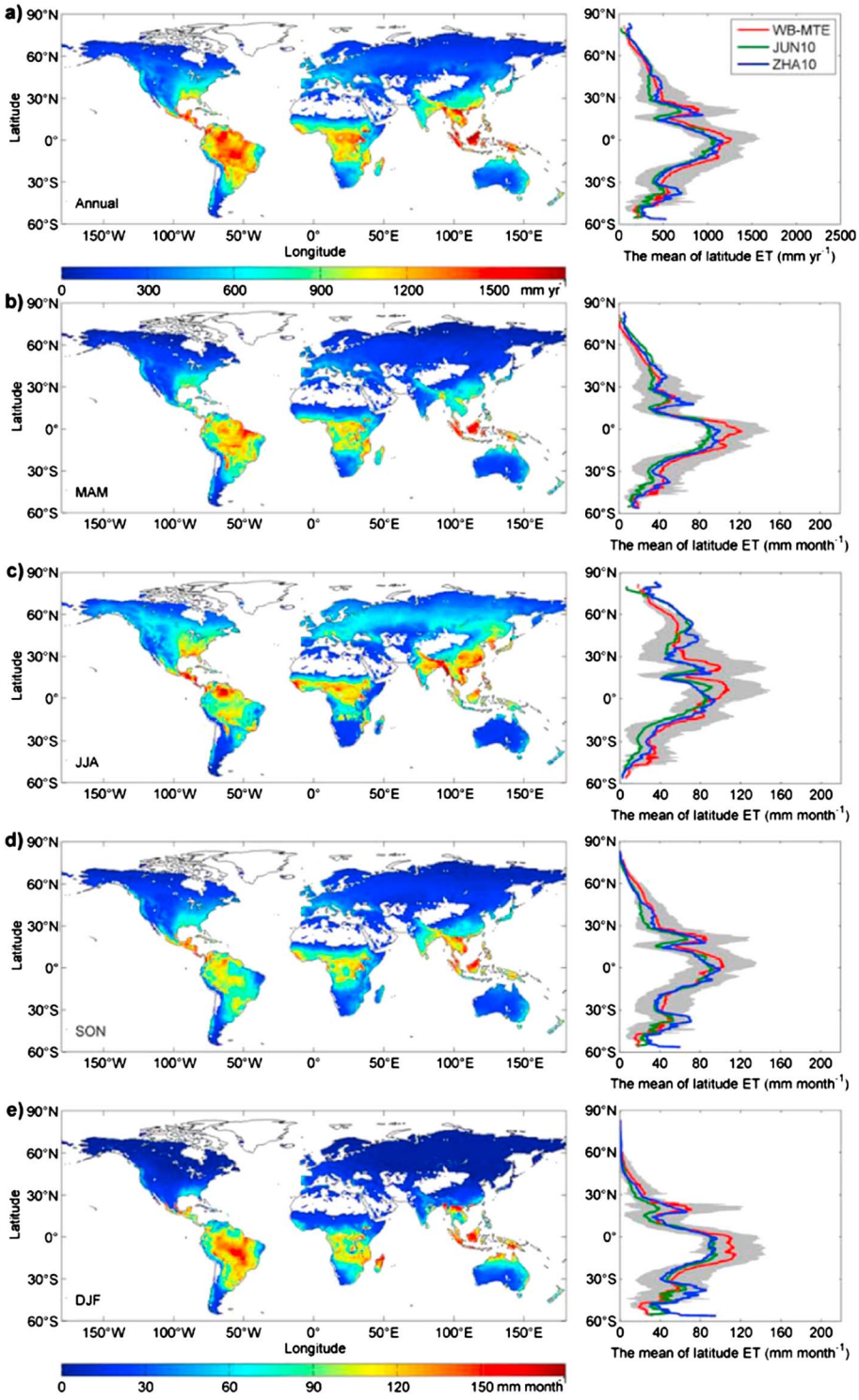

Figure 4. (left) Spatial patterns of multiyear average global land ET from the WB-MTE algorithm and (right) mean latitudinal distribution from 1982 to 2009: (a) Annual; (b) March, April, and May (MAM); (c) June, July, and August (JJA); (d) September, October, and November (SON); and (e) December, January, and February (DJF). The shaded area denotes 1 standard deviation of WB-MTE-simulated ET. Also shown are mean latitudinal ET from JUN10 and ZHA10.

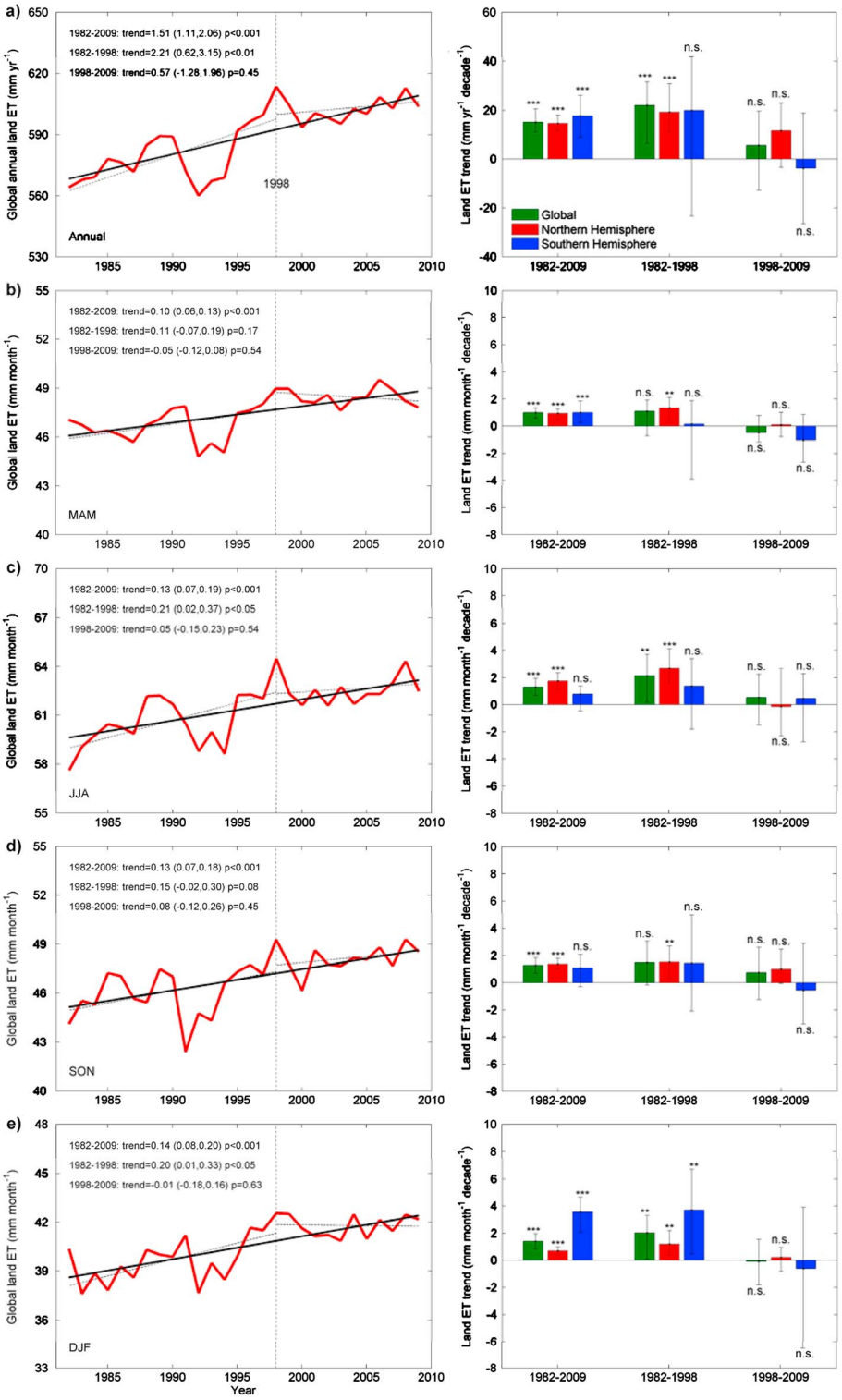

Figure 5. (left) Interannual variability of global land ET from 1982 to 2009 and (right) ET changes averaged over the globe, Northern Hemisphere, and Southern Hemisphere: (a) Annual; (b) March, April, and May (MAM); (c) June, July, and August (JJA); (d) September, October, and November (SON); and (e) December, January, and February (DJF). The numbers in parentheses are 95% confidence levels for trends based on Mann-Kendall test. The range of bars denotes the 95% confidence interval. Significance levels are indicated in 3 stars, 2 stars, and n.s. representing $p < 0.01$, $p < 0.05$, and $p > 0.05$, respectively.

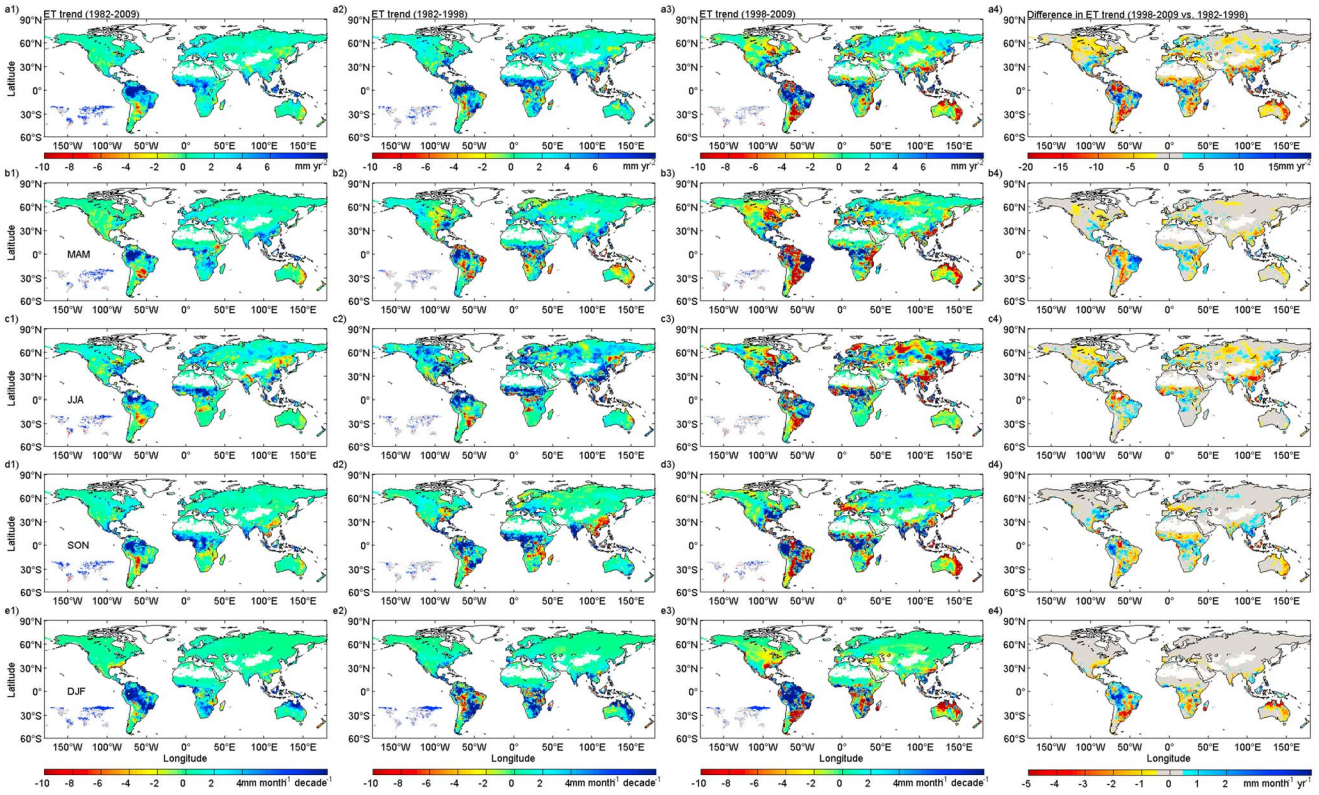

Figure 6. (first column) Spatial distributions of ET trends during 1982–2009, (second column) during 1982–1998, (third column) during 1998–2009, and (fourth column) spatial distribution of the difference in ET trend between periods 1982–1998 and 1998–2009: (a) Annual; (b) March, April, and May (MAM); (c) June, July, and August (JJA); (d) September, October, and November (SON); and (e) December, January, and February (DJF). The inset panels show the area where the ET trend is statistically significant ($p < 0.05$), and the blue stands for significant increase and the red for significant decrease.

significant positive trend after 1998 (0.1 mm month^{-1} yr^{-1}, $p = 0.54$). In DJF, global ET increased at a rate of 0.2 mm month^{-1} yr^{-1} before 1998 ($p < 0.05$), whereas the trend becomes negative and nonsignificant after 1998 (-0.01 mm month^{-1} yr^{-1}, $p = 0.63$).

A seasonal comparison of changes in ET trend before versus after 1998 indicates that the magnitudes of the ET trend changes during JJA and DJF are higher than in MAM and SON (Figures 5b–5e). Moreover, the sum of the changes in ET trend between pre-1998 and post-1998 periods during both JJA and DJF can account for 61% of the total annual ET trend change (Figures 5b–5e). Further, as seen in Figures 5c and 5e, the ET trend changes diagnosed during JJA mainly occur in the Northern Hemisphere (NH), whereas those during DJF occur in the Southern Hemisphere (SH). These patterns indicate that the trend changes in global ET (Figure 5a) mainly originate from the summer seasons in each hemisphere.

3.5. Spatial Patterns of ET Trend Changes

3.5.1. Annual

Figure 6a1 shows the spatial distribution of ET trends from 1982 to 2009. Eighty-five percent of the pixels show an increasing trend in ET (45% with a significant trend). The largest ET increases occurred in South America, Africa, and Southeast Asia (Figure 6a1), where annual ET is also the highest, as shown in Figure 4a. In addition, we diagnose a significant and widespread ET increase in the boreal region (Figure 6a1).

Over most of the globe, the overall increase in annual ET from 1982 to 2009 can largely be attributed to an increase that occurred before 1998 (Figure 6a2). After 1998, only a few regions still show this increasing ET trend: eastern Southern America, the rainforest of the Congo basin, and part of the Southeast Asian rainforest (Figure 6a3). Comparing annual ET trends for the periods before and after 1998, more and more pixels experienced a decreasing trend during the post-1998 period. This is particularly evident for Australia, southern Africa, southern South America, northern Amazonia, boreal North America, southern China, and the Korean

Peninsula and Japan (Figure 6a4). The spatial pattern of the difference in ET trends for each grid cell between the two time periods indicates a likelihood that the increase of annual ET has ceased, or even reversed, after 1998 (Figure 6a4) over 65% of the vegetated land surface, defined as NDVI > 0.1.

3.5.2. Seasonal

Figures 6b–6e show the spatial distribution of ET trends from 1982 to 2009 for each of the four seasons. The regions where maximum positive ET trends are reconstructed differ among the four seasons: areas with the highest positive ET trends are located around the equator during MAM and SON (Figures 6b and 6d), around the Tropic of Cancer in JJA (Figure 6c), and the Tropic of Capricorn in DJF (Figure 6e). During MAM and SON, ET increases significantly over the globe (22% and 27% of grid points with significant positive trends, respectively) ($p < 0.05$), especially in Eurasia. A large and significant trend is also found in the summer seasons in each hemisphere (JJA and DJF). Over tropical rainforest regions, increasing ET is found during each of the four seasons. By contrast, in some areas, e.g., eastern China, ET decreased in one season (SON) but increased in some other seasons (e.g., MAM).

We also analyzed changes in seasonal ET trends before and after 1998 and found that the spatial pattern of the change in ET trend has a strong seasonality (Figures 6b4, 6c4, 6d4, and 6e4). In JJA, the ET trend changes mainly occur over the NH, where more than 65% of pixels experienced a negative change of trend (Figure 6c4). In DJF, such negative trend changes mainly occurred in the SH, with 62% of pixels being affected (Figure 6e4). By contrast, during both MAM and SON, ET trend changes mainly occurred around the equator (~ 30°S to 30°N) (Figures 6b4 and 6d4). In general, the seasonal patterns of the ET trend changes after 1998 are similar to those of annual ET (see Figure 6a4). By comparing the spatial distributions of annual ET trend changes with those of seasonal trend changes, it can be seen that the annual ET trend change in the NH mainly originates from a change that happened in JJA, and the annual ET trend change in the SH mainly stems from a trend change during DJF (Figures 6c4 and 6e4). We should note that the trend change in the tropics is much more complex. For example, in Amazonia, the trend changes in the eastern and the western parts of the basin are completely different among the four seasons (Figure 6).

4. Discussion and Conclusion

4.1. Comparison With EC-Based ET Estimates

According to our WB-MTE reconstruction, ET and its trends are higher than the estimates from the MTE reconstruction based upon eddy-covariance measurements (JUN10), particularly in wet tropical regions (e.g., Figures 3b and 4). The discrepancies between the two methods can be further analyzed by splitting the whole year into dry and wet seasons. We define the *dry season* as having continuous months with multiyear averaged precipitation less than 30% of multiyear averaged annual precipitation and the other months as the *wet season* [*Staver et al*., 2011] (see Figures 7a and 7b). During the dry season, the latitudinal distributions of the WB-MTE and JUN10 ET agree well with each other ($R = 0.96$, $p < 0.001$) (Figure 7c). On the interannual timescale, the ET variability from WB-MTE is roughly consistent with JUN10 if the period 1991–1994 is excluded (Figure 8b). By contrast, during the wet season, WB-MTE ET is obviously higher (19 mm per month) than JUN10 ET over the tropics (23°S ~ 23°N) by on average 19% (Figure 7d). Moreover, WB-MTE ET has a much large interannual variability during the wet season than the JUN10 product (Figure 8c). Thus, the observed discrepancies between our WB-MTE and the eddy-covariance based JUN10 reconstruction (e.g., Figures 3b and 4) are driven primarily by their differences in the wet season. It is the same for the discrepancies between the WB-MTE and ZHA10, which is a satellite-based energy balance method parameterized using eddy-covariance measurements. Causes for these differences are discussed below.

First, solar radiation is recognized to be a key variable in determining ET especially in wet season regions where soil moisture is not limiting ET (e.g., wet tropics) [*Hutyra et al*., 2007; *Fisher et al*., 2009; *Costa et al*., 2010; *Wang and Dickinson*, 2012]. However, MTE in JUN10 did not include solar radiation as a predictor and ZHA10 used remotely sensed radiation input data with insufficient accuracy [*Yan et al*., 2012; *Zhang et al*., 2012]. Evidence for this can be found during the Pinatubo volcano eruption of 1991. The consequent reduction in solar radiation from 1991 to 1992 (decreased by 2.2 W m^{-2} globally) leads to a divergence between JUN10 and WB-MTE for this period (gray-shaded area in Figure 8). The abrupt decrease of ET is also confirmed by most other ET products from observation-based algorithms, land surface model simulations, and atmospheric reanalysis [see *Mueller et al*., 2013]. This difference in methodology is even more pronounced if only the wet season is considered

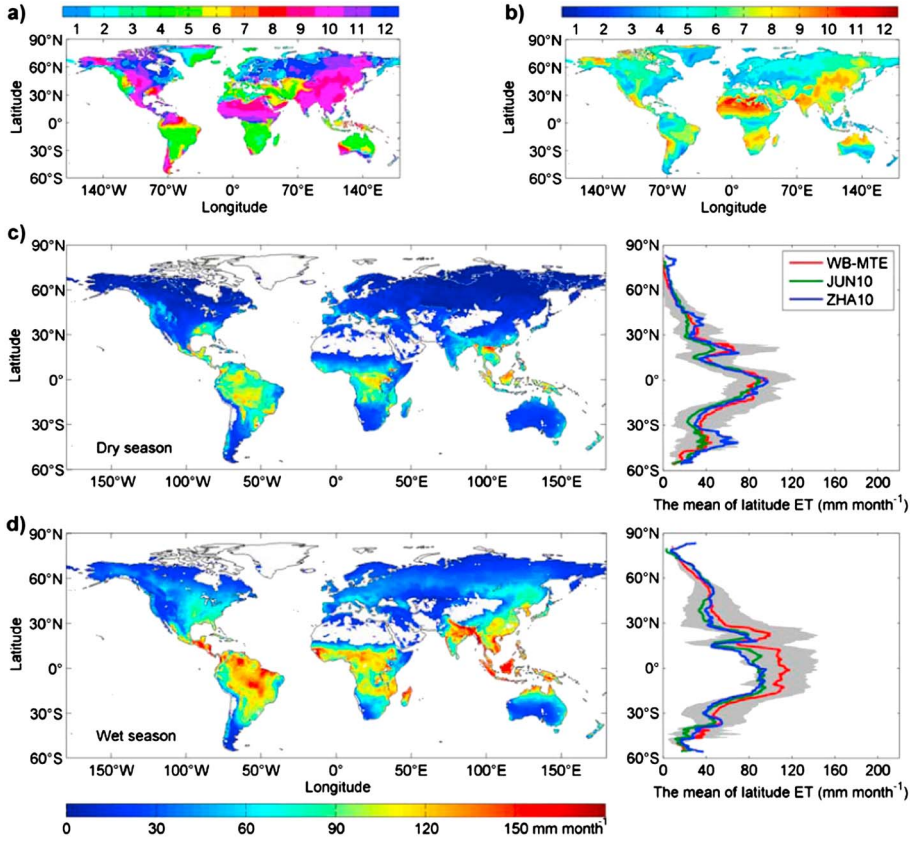

Figure 7. Spatial distributions of (a) the beginning of the dry season and (b) the length of dry season. Spatial distribution of (c) dry season averaged ET and (d) wet season averaged ET and mean latitudinal ET estimated from three different methods (WB-MTE, JUN10, and ZHA10). The shaded area denotes 1 standard deviation of ET from WB-MTE.

(Figure 8). This leads to a limitation in the capacity of the two EC-based methods to simulate interannual or decadal variations in ET, a conclusion that has also been drawn by previous studies [*Yan et al.*, 2012; *Zhang et al.*, 2012]. Second, forest rainfall interception loss is an important component of ET under wet canopy conditions (e.g., wet tropical rainforest). The low aerodynamic resistance and the water supply unrestrained by stomatal control result in high evaporation rates from wet canopies [*Gash*, 1979; *Miralles et al.*, 2010, 2011]. This process could result in a higher ET during the wet season [*Schellekens et al.*, 1999]. For example, at a Bornean tropical rainforest station, the ET was found to be as high as 129 mm per month that is similar to the WB-MTE ET during the wet season (Figure 7d), and its canopy rainfall interception loss up to 30% of the transpiration and 23% of total ET [*Kumagai et al.*, 2005]. However, eddy-covariance measurements may underestimate wet canopy evaporation (rainfall interception loss) over the tropics due to the intermittency of the strong turbulence during rainfall [*Holwerda et al.*, 2012]. Moreover, the canopy interception loss process is not considered in the global ET algorithm of ZHA10. This might be an important reason for the striking difference between the water balance ET and the EC-based ET for the wet tropics.

Third, we should note that other factors also contribute to uncertainties in ET trend or variability reconstructed by both JUN10 and ZHA10. In particular, the MTE method of JUN10 was trained with data from EC sites with an average duration of only 2 years [*Jung et al.*, 2010; *Zhang et al.*, 2012], and it thus relies on spatial (current) gradients to reconstruct temporal trends. In contrast, the WB-estimated basin ET applied to train MTE spans the period of GRACE data, beginning in 2002. While this period is much longer than that used by JUN10, it still suffers from the assumptions in a "space-for-time" substitution. In addition, the ET underestimation by EC-based approaches in the tropics, which is also documented in a recent modeling study [*Shi et al.*, 2013], might also stem from the fact that FLUXNET has a relatively sparse spatial coverage of EC sites in the tropics [*Wang and Dickinson*, 2012].

Finally, we should note that the WB-estimated basin ET is a whole basin average, which includes evaporation from lakes and river as well. Water bodies account for nearly 2% of the area across all 95 basins used in this

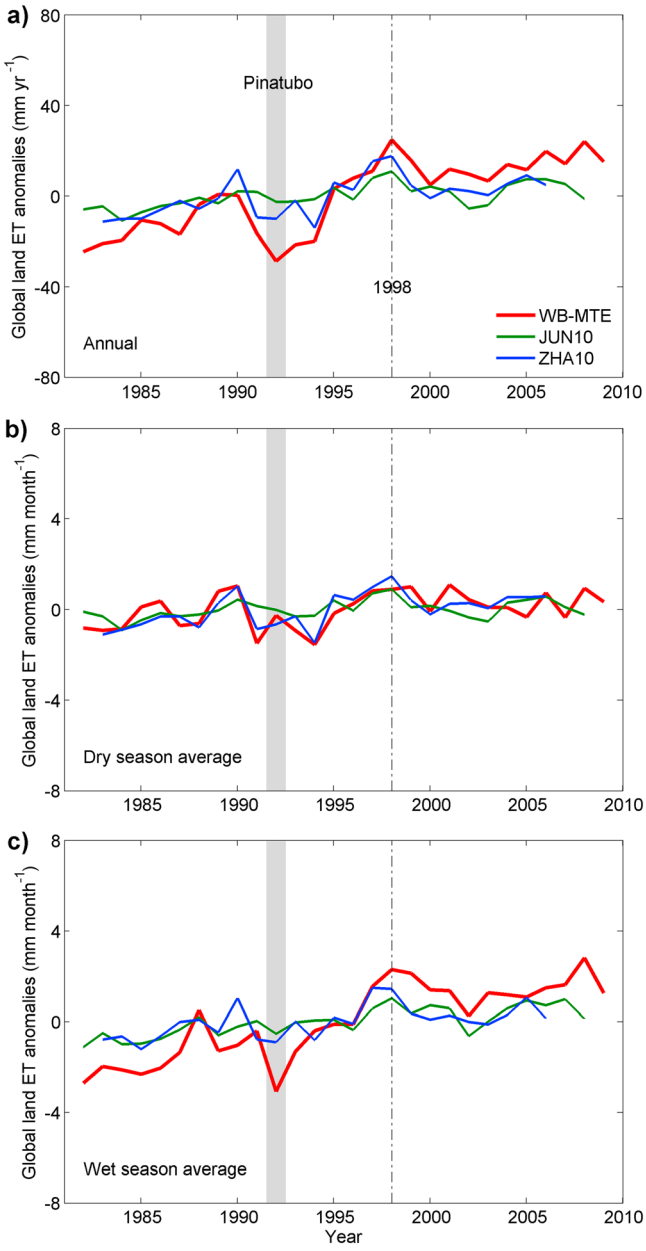

Figure 8. Comparison of interannual anomalies of global (a) annual, (b) dry season average, and (c) wet season average ET between 1982 and 2009 among the three approaches (WB-MTE, JUN10, and ZHA10).

study. Our MTE method trained with WB basin ET measurements might thus be expected to overestimate ET on a global scale. However, this seems unlikely, because the WB-MTE-based ET is only higher than other approaches over the tropics during the wet season (see Figures 3, 4, and 7).

4.2. Change in Global Land ET Trends

The WB-MTE reconstruction confirms previous findings that global annual land ET has increased during the last two decades of the twentieth century [*Jung et al.*, 2010; *Zhang et al.*, 2012] and that this trend has ceased over the past decade [*Jung et al.*, 2010; *Vinukollu et al.*, 2011; *Mueller et al.*, 2013]. *Jung et al.* [2010] proposed that the change in trend is the result of an increasingly widespread limitation of ET by lack of soil moisture.

In this study, we employ two soil moisture data sets: total soil moisture content (in the depth of soil down to 2.89 m) from ERA-Interim reanalysis [*Dee et al.*, 2011] and top soil moisture (in the top ~20 mm) from the ESA-CCI SM

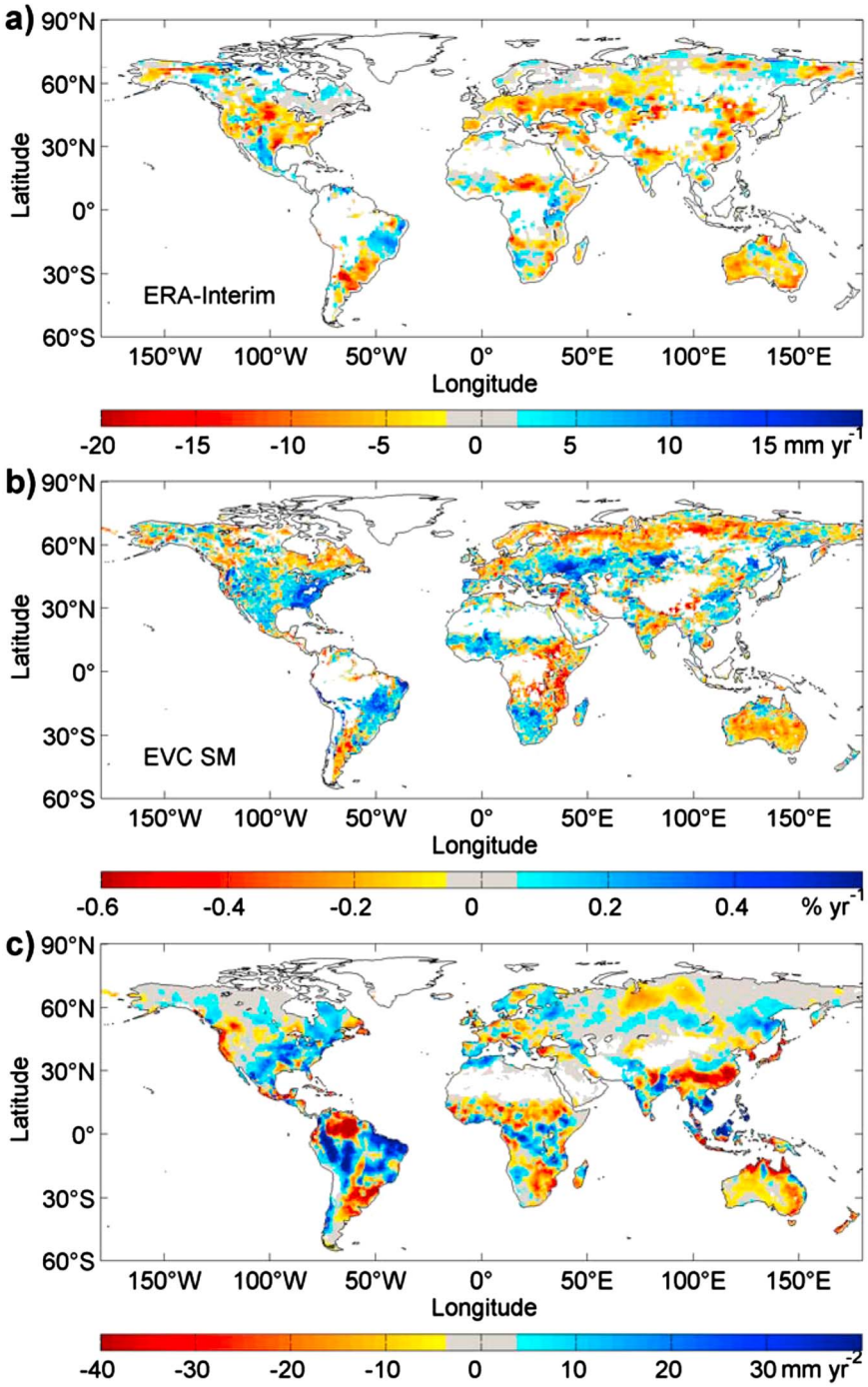

Figure 9. Spatial patterns of the trend change between 1982–1998 and 1998–2008 in (a) ERA-interim derived soil moisture (in millimeters and to a depth of 2890 mm), (b) EVC SM-derived soil moisture (in percentage and in the depth of ~20 mm), and between 1982–1998 and 1998–2009 in (c) CRU precipitation. Small trend changes are shown in gray to enhance clarity.

data set; the latter obtained by a fusion of passive and active satellite observations [*Dorigo et al.*, 2012]. We find a strong spatial correlation between the trend changes of WB-MTE ET and the trend changes of the two soil moisture data sets, particularly in the SH ($p < 0.001$; Figures 9a and 9b). This is also documented by *Jung et al.* [2010]. In the NH, spatial consistency is also found between WB-MTEET trend changes and soil moisture trend changes from ERA-Interim (Figures 6a4 and 9a) but not for surface soil moisture from remote sensing (Figures 6a4 and 9b). This discrepancy may result from the different depths of soil moisture in the two data sets,

since the satellite approach only detects moisture in the top ~20 mm of soil. For example, there is more deep-rooted (>20 mm) vegetation in the NH [*Jackson et al.*, 1996], particularly in boreal forest, than in the SH, and because vegetation can extract water from the whole layer of soil, it is possible that ET in the NH is more regulated by the total soil moisture. On the other hand, our results show that the cessation of the positive ET trend since 1998 mainly occurs over the summer hemispheres (Figures 5b–5e) when the energy supply is relatively abundant. This implies that soil moisture rather than energy supply may become the limiting control on ET and be responsible for the changes in ET trends [*Fischer et al.*, 2007; *Teuling et al.*, 2009; *Jung et al.*, 2010].

We also find a strong spatial coherence between precipitation trend changes and ET trend changes ($R = 0.82$, $p < 0.001$) over the past three decades (Figures 6a4 and 9c). This coherence may be explained by the fact that less precipitation leads to lower soil moisture (also see Figures 9a and 9b), which in turn limits ET (see Figure 6a4). In addition, ET can also feedback positively on precipitation since the precipitated water in the atmosphere is partly formed from water evaporated from the land surface, although the strength of this impact is still not clear [*Eltahir and Bras*, 1994; *Koster et al.*, 2003, 2004; *Seneviratne et al.*, 2010; *Findell et al.*, 2011]. If this impact were very strong, a reduced ET due to limiting soil moisture would decrease the precipitation, which should further reduce soil moisture [*Koster et al.*, 2004; *Seneviratne et al.*, 2010]. This is the mechanism for a positive feedback between ET and soil moisture, implying that both ET and soil moisture might continue to decline once a deficit in soil moisture is established. This feedback process could provide a mechanism that would attenuate acceleration of the global hydrological cycle due to recent global warming [*Koster et al.*, 2003; *Jung et al.*, 2010; *Teuling et al.*, 2013]. On the other hand, the feedback of ET on precipitation may not be so large [*Seneviratne et al.*, 2010], for example, a recent study showed that the stalled increase in the trend of increasing global land precipitation since the late 1990s is mainly due to the increasing levels of stratospheric aerosols [*Fyfe et al.*, 2013]. If this is true, then a positive feedback between soil moisture and ET is perhaps of less importance, and the recent ET decline may then not trigger a permanent "braking effect" on the terrestrial hydrological cycle. However, this issue is still not clear and needs further investigation [see also *Salvucci et al.*, 2002; *Koster et al.*, 2003, 2004; *Jung et al.*, 2010; *Seneviratne et al.*, 2010].

To summarize, we have developed a water balance approach (WB) in a machine-learning algorithm (MTE) (referred to as WB-MTE) to estimate basin ET at the monthly timescale. We then provided an estimate of global ET over the past three decades by integrating satellite remote sensing, surface meteorological observations, and the WB-MTE algorithm. A strength of this data-driven approach in modeling ET is that it does not require any model assumptions. However, we note that because the WB-MTE algorithm is a statistical tool, the relative importance of different variables or processes in determining ET cannot be readily disentangled. Thus, process-based models including the main drivers of ET are also needed to understand the relative contributions of the different factors (e.g., climate, atmospheric CO_2 concentration, nitrogen deposition, aerosol deposition, and land use change) influencing the spatial and temporal variations in ET at different timescales [e.g., *Koster et al.*, 2004; *Teuling et al.*, 2009; *Shi et al.*, 2013].

Acknowledgments
We thank M. Jung for helpful comments and the Global Runoff Data Centre (GRDC) for runoff data. This study was supported by the National Natural Science Foundation of China (grant 41125004), National Basic Research Program of China (2013CB956303), and National Youth Top-notch Talent Support Program in China.

References

Baldocchi, D., et al. (2001), FLUXNET: A new tool to study the temporal and spatial variability of ecosystem-scale carbon dioxide, water vapor, and energy flux densities, *Bull. Am. Meteorol. Soc.*, *82*(11), 2415–2434.

Bruinsma, S., J. Lemoine, R. Biancale, and N. Valès (2010), CNES/GRGS 10-day gravity field models (release 2) and their evaluation, *Adv. Space Res.*, *45*(4), 587–601, doi:10.1016/j.asr.2009.10.012.

Cohen, W. B., T. K. Maiersperger, D. P. Turner, W. D. Ritts, D. Pflugmacher, R. E. Kennedy, A. Kirschbaum, S. W. Running, M. Costa, and S. T. Gower (2006), MODIS land cover and LAI collection 4 product quality across nine sites in the western hemisphere, *IEEE Trans. Geosci. Remote Sens.*, *44*(7), 1843–1857, doi:10.1109/tgrs.2006.876026.

Costa, M. H., M. C. Biajoli, L. Sanches, A. C. M. Malhado, L. R. Hutyra, H. R. da Rocha, R. G. Aguiar, and A. C. de Araújo (2010), Atmospheric versus vegetation controls of Amazonian tropical rain forest evapotranspiration: Are the wet and seasonally dry rain forests any different?, *J. Geophys. Res.*, *115*, G04021, doi:10.1029/2009JG001179.

Dee, D. P., et al. (2011), The ERA-Interim reanalysis: Configuration and performance of the data assimilation system, *Q. J. R. Meteorol. Soc.*, *137*(656), 553–597, doi:10.1002/qj.828.

Dorigo, W., R. de Jeu, D. Chung, R. Parinussa, Y. Liu, W. Wagner, and D. Fernández-Prieto (2012), Evaluating global trends (1988–2010) in harmonized multi-satellite surface soil moisture, *Geophys. Res. Lett.*, *39*, L18405, doi:10.1029/2012GL052988.

Douville, H., A. Ribes, B. Decharme, R. Alkama, and J. Sheffield (2013), Anthropogenic influence on multidecadal changes in reconstructed global evapotranspiration, *Nat. Clim. Change*, *3*(1), 59–62, doi:10.1038/nclimate1632.

Eltahir, E. A. B., and R. L. Bras (1994), Precipitation recycling in the Amazon basin, *Q. J. R. Meteorol. Soc.*, *120*(518), 861–880, doi:10.1002/qj.49712051806.

Findell, K. L., P. Gentine, B. R. Lintner, and C. Kerr (2011), Probability of afternoon precipitation in eastern United States and Mexico enhanced by high evaporation, *Nat. Geosci.*, *4*(7), 434–439, doi:10.1038/ngeo1174.

Fischer, E. M., S. I. Seneviratne, P. L. Vidale, D. Lüthi, and C. Schär (2007), Soil moisture–atmosphere interactions during the 2003 European summer heat wave, *J. Clim.*, *20*(20), 5081–5099, doi:10.1175/JCLI4288.1.

Fisher, J. B., et al. (2009), The land–atmosphere water flux in the tropics, *Global Change Biol.*, *15*(11), 2694–2714, doi:10.1111/j.1365-2486.2008.01813.x.

Fisher, J. B., R. J. Whittaker, and Y. Malhi (2011), ET come home: Potential evapotranspiration in geographical ecology, *Global Ecol. Biogeogr.*, *20*(1), 1–18, doi:10.1111/j.1466-8238.2010.00578.x.

Foken, T. (2008), The energy balance closure problem: An overview, *Ecol. Appl.*, *18*(6), 1351–1367, doi:10.1890/06-0922.1.

Fyfe, J. C., K. von Salzen, J. N. S. Cole, N. P. Gillett, and J. P. Vernier (2013), Surface response to stratospheric aerosol changes in a coupled atmosphere-ocean model, *Geophys. Res. Lett.*, *40*, 584–588, doi:10.1002/grl.50156.

Gash, J. H. C. (1979), An analytical model of rainfall interception by forests, *Q. J. R. Meteorol. Soc.*, *105*(443), 43–55.

GRDC (2007), *Major River Basins of the World/Global Runoff Data Centre*, edited by Federal Institute of Hydrology (BfG), Koblenz, Germany.

Holwerda, F., L. A. Bruijnzeel, F. N. Scatena, H. F. Vugts, and A. G. C. A. Meesters (2012), Wet canopy evaporation from a Puerto Rican lower montane rain forest: The importance of realistically estimated aerodynamic conductance, *J. Hydrol.*, *414–415*(0), 1–15, doi:10.1016/j.jhydrol.2011.07.033.

Huntington, T. G. (2006), Evidence for intensification of the global water cycle: Review and synthesis, *J. Hydrol.*, *319*(1–4), 83–95, doi:10.1016/j.jhydrol.2005.07.003.

Hutyra, L. R., J. W. Munger, S. R. Saleska, E. Gottlieb, B. C. Daube, A. L. Dunn, D. F. Amaral, P. B. de Camargo, and S. C. Wofsy (2007), Seasonal controls on the exchange of carbon and water in an Amazonian rain forest, *J. Geophys. Res.*, *112*, G03008, doi:10.1029/2006JG000365.

Jackson, R. B., J. Canadell, J. R. Ehleringer, H. A. Mooney, O. E. Sala, and E. D. Schulze (1996), A global analysis of root distributions for terrestrial biomes, *Oecologia*, *108*(3), 389–411, doi:10.1007/bf00333714.

Jung, M., M. Reichstein, and A. Bondeau (2009), Towards global empirical upscaling of FLUXNET eddy covariance observations: Validation of a model tree ensemble approach using a biosphere model, *Biogeosciences*, *6*(10), 2001–2013, doi:10.5194/bg-6-2001-2009.

Jung, M., et al. (2010), Recent decline in the global land evapotranspiration trend due to limited moisture supply, *Nature*, *467*(7318), 951–954, doi:10.1038/nature09396.

Kalma, J. D., T. R. McVicar, and M. F. McCabe (2008), Estimating land surface evaporation: A review of methods using remotely sensed surface temperature data, *Surv. Geophys.*, *29*(4-5), 421–469, doi:10.1007/s10712-008-9037-z.

Kanamitsu, M., W. Ebisuzaki, J. Woollen, S. K. Yang, J. J. Hnilo, M. Fiorino, and G. L. Potter (2002), NCEP-DOE AMIP-II reanalysis (R-2), *Bull. Am. Meteorol. Soc.*, *83*(11), 1631–1643, doi:10.1175/bams-83-11-1631.

Koster, R. D., M. J. Suarez, R. W. Higgins, and H. M. Van den Dool (2003), Observational evidence that soil moisture variations affect precipitation, *Geophys. Res. Lett.*, *30*(5), 1241, doi:10.1029/2002GL016571.

Koster, R. D., et al. (2004), Regions of strong coupling between soil moisture and precipitation, *Science*, *305*(5687), 1138–1140, doi:10.1126/science.1100217.

Kumagai, T. O., T. M. Saitoh, Y. Sato, H. Takahashi, O. J. Manfroi, T. Morooka, K. Kuraji, M. Suzuki, T. Yasunari, and H. Komatsu (2005), Annual water balance and seasonality of evapotranspiration in a Bornean tropical rainforest, *Agric. For. Meteorol.*, *128*(1–2), 81–92, doi:10.1016/j.agrformet.2004.08.006.

McVicar, T. R., et al. (2012), Global review and synthesis of trends in observed terrestrial near-surface wind speeds: Implications for evaporation, *J. Hydrol.*, *416–417*, 182–205, doi:10.1016/j.jhydrol.2011.10.024.

Miralles, D. G., J. H. Gash, T. R. H. Holmes, R. A. M. de Jeu, and A. J. Dolman (2010), Global canopy interception from satellite observations, *J. Geophys. Res.*, *115*, D16122, doi:10.1029/2009JD013530.

Miralles, D. G., R. A. M. De Jeu, J. H. Gash, T. R. H. Holmes, and A. J. Dolman (2011), Magnitude and variability of land evaporation and its components at the global scale, *Hydrol. Earth Syst. Sci.*, *15*(3), 967–981, doi:10.5194/hess-15-967-2011.

Mitchell, T. D., and P. D. Jones (2005), An improved method of constructing a database of monthly climate observations and associated high-resolution grids, *Int. J. Climatol.*, *25*(6), 693–712, doi:10.1002/joc.1181.

Monteith, J. L. (1981), Evaporation and surface temperature, *Q. J. R. Meteorol. Soc.*, *107*(451), 1–27.

Mu, Q., M. Zhao, and S. W. Running (2011), Improvements to a MODIS global terrestrial evapotranspiration algorithm, *Remote Sens. Environ.*, *115*(8), 1781–1800, doi:10.1016/j.rse.2011.02.019.

Mueller, B., et al. (2011), Evaluation of global observations-based evapotranspiration datasets and IPCC AR4 simulations, *Geophys. Res. Lett.*, *38*, L06402, doi:10.1029/2010GL046230.

Mueller, B., et al. (2013), Benchmark products for land evapotranspiration: LandFlux-EVAL multi-dataset synthesis, *Hydrol. Earth Syst. Sci. Discuss.*, *10*(1), 769–805, doi:10.5194/hessd-10-769-2013.

Myneni, R. B., C. J. Tucker, G. Asrar, and C. D. Keeling (1998), Interannual variations in satellite-sensed vegetation index data from 1981 to 1991, *J. Geophys. Res.*, *103*(D6), 6145–6160, doi:10.1029/97JD03603.

Penman, H. L. (1948), Natural evaporation from open water, bare soil and grass, *Proc. R. Soc. London, Ser. A*, *193*(1032), 120–145.

Piao, S., P. Friedlingstein, P. Ciais, N. de Noblet-Ducoudré, D. Labat, and S. Zaehle (2007), Changes in climate and land use have a larger direct impact than rising CO_2 on global river runoff trends, *Proc. Natl. Acad. Sci. U. S. A.*, *104*(39), 15,242–15,247, doi:10.1073/pnas.0707213104.

Rodell, M., J. S. Famiglietti, J. Chen, S. I. Seneviratne, P. Viterbo, S. Holl, and C. R. Wilson (2004), Basin scale estimates of evapotranspiration using GRACE and other observations, *Geophys. Res. Lett.*, *31*, L20504, doi:10.1029/2004GL020873.

Roderick, M. L., L. D. Rotstayn, G. D. Farquhar, and M. T. Hobbins (2007), On the attribution of changing pan evaporation, *Geophys. Res. Lett.*, *34*, L17403, doi:10.1029/2007GL031166.

Salvucci, G. D., J. A. Saleem, and R. Kaufmann (2002), Investigating soil moisture feedbacks on precipitation with tests of Granger causality, *Adv. Water Resour.*, *25*(8–12), 1305–1312, doi:10.1016/S0309-1708(02)00057-X.

Schellekens, J., F. N. Scatena, L. A. Bruijnzeel, and A. J. Wickel (1999), Modelling rainfall interception by a lowland tropical rain forest in northeastern Puerto Rico, *J. Hydrol.*, *225*(3–4), 168–184, doi:10.1016/S0022-1694(99)00157-2.

Seneviratne, S. I., T. Corti, E. L. Davin, M. Hirschi, E. B. Jaeger, I. Lehner, B. Orlowsky, and A. J. Teuling (2010), Investigating soil moisture–climate interactions in a changing climate: A review, *Earth Sci. Rev.*, *99*(3–4), 125–161, doi:10.1016/j.earscirev.2010.02.004.

Sheffield, J., E. F. Wood, and M. L. Roderick (2012), Little change in global drought over the past 60 years, *Nature*, *491*(7424), 435–438, doi:10.1038/nature11575.

Shi, X. Y., J. F. Mao, E. T. Peter, and M. Y. Huang (2013), Spatiotemporal patterns of evapotranspiration in response to multiple environmental factors simulated by the Community Land Model, *Environ. Res. Lett.*, *8*, 024,012, doi:10.1088/1748-9326/8/2/024012.

Staver, A. C., S. Archibald, and S. A. Levin (2011), The global extent and determinants of savanna and forest as alternative biome states, *Science*, *334*(6053), 230–232, doi:10.1126/science.1210465.

Tapley, B. D., S. Bettadpur, J. C. Ries, P. F. Thompson, and M. M. Watkins (2004), GRACE measurements of mass variability in the earth system, *Science*, *305*(5683), 503–505, doi:10.1126/science.1099192.

Teuling, A. J., et al. (2009), A regional perspective on trends in continental evaporation, *Geophys. Res. Lett.*, *36*, L02404, doi:10.1029/2008GL036584.

Teuling, A. J., A. van Loon, S. I. Seneviratne, I. Lehner, M. Aubinet, B. Heinesch, C. Bernhofer, T. Grünwald, H. Prasse, and U. Spank (2013), Evapotranspiration amplifies European summer drought, *Geophys. Res. Lett.*, *40*, 2071–2075, doi:10.1002/grl.50495.

Thornthwaite, C. W. (1948), An approach toward a rational classification of climate, *Geogr. Rev.*, *38*(1), 55–94.

Trenberth, K. E., J. T. Fasullo, and J. Kiehl (2009), Earth's global energy budget, *Bull. Am. Meteorol. Soc.*, *90*(3), 311–323, doi:10.1175/2008bams2634.1.

Tucker, C., J. Pinzon, M. Brown, D. Slayback, E. Pak, R. Mahoney, E. Vermote, and N. El Saleous (2005), An extended AVHRR 8 km NDVI dataset compatible with MODIS and SPOT vegetation NDVI data, *Int. J. Remote Sens.*, *26*(20), 4485–4498, doi:10.1080/01431160500168686.

Vinukollu, R. K., R. Meynadier, J. Sheffield, and E. F. Wood (2011), Multi-model, multi-sensor estimates of global evapotranspiration: Climatology, uncertainties and trends, *Hydrol. Processes*, *25*(26), 3993–4010, doi:10.1002/hyp.8393.

Wang, K., and R. E. Dickinson (2012), A review of global terrestrial evapotranspiration: Observation, modeling, climatology, and climatic variability, *Rev. Geophys.*, *50*, RG2005, doi:10.1029/2011RG000373.

Wang, K., R. E. Dickinson, M. Wild, and S. Liang (2010), Evidence for decadal variation in global terrestrial evapotranspiration between 1982 and 2002: 2. Results, *J. Geophys. Res.*, *115*, D20113, doi:10.1029/2010JD013847.

Wilson, K., et al. (2002), Energy balance closure at FLUXNET sites, *Agric. For. Meteorol.*, *113*(1–4), 223–243, doi:10.1016/s0168-1923(02)00109-0.

Yan, H., et al. (2012), Global estimation of evapotranspiration using a leaf area index-based surface energy and water balance model, *Remote Sens. Environ.*, *124*, 581–595, doi:10.1016/j.rse.2012.06.004.

Zeng, Z. Z., S. L. Piao, X. Lin, G. D. Yin, S. S. Peng, P. Ciais, and R. B. Myneni (2012), Global evapotranspiration over the past three decades: Estimation based on the water balance equation combined with empirical models, *Environ. Res. Lett.*, *7*, 014,026, doi:10.1088/1748-9326/7/1/014026.

Zhang, K., J. S. Kimball, R. R. Nemani, and S. W. Running (2010), A continuous satellite-derived global record of land surface evapotranspiration from 1983 to 2006, *Water Resour. Res.*, *46*, W09522, doi:10.1029/2009WR008800.

Zhang, Y., R. Leuning, F. H. S. Chiew, E. Wang, L. Zhang, C. Liu, F. Sun, M. C. Peel, Y. Shen, and M. Jung (2012), Decadal trends in evaporation from global energy and water balances, *J. Hydrometeorol.*, *13*(1), 379–391, doi:10.1175/jhm-d-11-012.1.